Parallel Architecture of a Frequency Comb Qudit Quantum Processor

Duncan L. MacFarlane, Hiva Shahoei, R. Mason Tuller, Cooper Shapard, Caden Crowson, and Mitchell A. Thornton
The Darwin Deason Institute for Cybersecurity
and
Department of Electrical and Computer Engineering
The Bobby B. Lyle School of Engineering
Southern Methodist University
Dallas, Texas, USA
{dmarcfarlane, hshahoei, mtuller, cshapard, ccrowson, mitch}@smu.edu

***Abstract*—Quantum optical frequency combs provide an intriguing approach to high-dimensional quantum states. Because of the need to move probability amplitudes among different colors, the realization of gates appropriate to multicolor photons requires nonlinear or electro-optic mixing. This paper describes a novel architecture for such gates. The parallel arrangement of mixers allows graceful scaling beyond two-dimensional qubits to higher dimension qudits, and this enables multivalue quantum logic. The parallelism of the implementation simplifies the programming of the gate for a particular operation. As an example, we demonstrate the design of a four-dimensional Chrestenson operator.**

***Index Terms*—Integrated Photonics; Multicolor Photons, Quantum Informatics. High Radix Qudits**

I. Introduction

When one articulates photonic quantum processing with polarization-encoded qubits, components such as waveplates, beamsplitters, and polarizers are employed. Similarly, quantum circuits for spatially encoded photonic qudits use couplers, interferometers, ring resonators, and combiners. The transfer functions for all the components identified so far, and hence the circuits they enable, are linear and time-invariant (LTI). Multicolor photons provide a promising route to higher-dimensional qudits, and hence to multivalued quantum logic. Working with multicolor photon states, however, requires the movement of probability amplitudes among the colors (wavelengths or frequencies) [1–7]. LTI components will not accomplish this task. Consequently, nonlinear optics effects, or more commonly, mixing, become necessary operations in the construction of quantum gates for multicolored photon qubits and qudits. In many works to date, phase modulators enable the mixing of photon colors, and linear time-invariant filters adjust the amplitude and phases of the components produced by the RF electro-optic modulators [5, 8–15]. The purpose of this paper is to present an alternative to the predominantly serial architecture of EOMs and LTI filters favored to date to realize quantum logic gates for processing multicolor photon states. The architecture described herein scales gracefully to states of higher dimension, providing a flexible platform for advanced quantum information processing. Higher-dimensional quantum states, or qudits, align naturally with multiple-valued logic (MVL) principles, where information is processed using more than two discrete levels. Quantum computing using qudits of dimension higher than two can offer performance and application benefits beyond those when using standard, two-dimensional qubits [22]. For instance, a radix-4 qudit corresponds to quaternary logic, potentially offering advantages in computational efficiency and circuit complexity reduction, analogous to benefits seen in classical MVL systems [23]. The parallelism of the implementation simplifies the programming of the gate for a particular operation. As an example, we demonstrate the design of a four-dimensional Chrestenson operator, which generalizes the Hadamard gate to higher radices and is foundational in MVL spectral methods. The architecture described herein scales gracefully to states of higher dimension, has a desirable geometry and footprint when implemented as a quantum photonic integrated circuit (QPIC) cell, and has a preferable overall loss characteristic in comparison to the "quantum Fourier processor" (QFP) architecture as described in [10, 12, 13].

II. A Parallel Architecture

In this work, two modifications of past circuits [10, 12, 13] are employed. LTI filters and Electro-optic modulators are still deployed; however, more complicated modulators – Mach-Zehnder Modulators (MZMs) and nested MZMs – are brought to bear. Secondly, these integrated mixers and filters are arranged in a parallel architecture. This is shown in Figure 1.

An input multicolor photon state enters the quantum gate from the left. In a manner similar to the grating in the programmable filter in [10, 12, 13], a demultiplexer (DeMUX) parallelizes the constituent frequencies (color components). Since most multicolor photon states entail combs of frequencies defined by some free spectral range (FSR) of the generation component, the DeMUX may be realized with LTI filters, ring resonators, or cascades of Mach-Zehnder Interferometers (MZIs). The former is an infinite input response (IIR) filter, and this has ramifications for the effects of its group delay. The latter, finite impulse response (FIR) filter may require a multi-

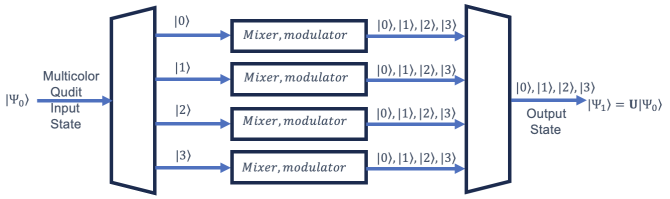

Fig. 1: Qudit quantum frequency processor. A four color qudit is input to the gate. A demux separates the colors and the demultiplexed components are mixed in a parallel arrangement of MZMs. The mixed components exit the gate through a mux. While a four-dimensional state is illustrated, more mixers may be added in parallel to scale gracefully to higher dimension.

plicity of stages to achieve a desired frequency discrimination, with concomitant overheads of control and parasitic losses. In either case, knowledge of the comb frequency spacing greatly simplifies this DeMUX. Each frequency component is then modulated by a specified RF signal, $m(t)$. For a K-order quantum state, each RF modulating signal typically comprises $(K-1)$ cosine components, each with designated amplitudes and phases. Since the MZMs and nested MZMs have multiple arms, each electro-optic segment may be driven by its own appropriate RF cosine Fourier series. Thus, the amplitude and phases provide degrees of freedom that may be designed to achieve the required transfer matrix of the gate at issue. A final weight and phase may be assigned to each frequency of the multicolor photon before multiplexing together to provide the gate's output state $|\Psi\rangle$. The use of MZMs integrates mixing and filtering functionalities, since an MZM is a time-varying FIR filter. Thus, the architecture combines the mixing and filtering operations that are distinct in the serial architectures of [10, 12, 13].

III. The Realization of a Chrestenson ($\mathbf{C_4}$) Gate

As an illustration of the architecture, and its applicability to states with dimension higher than 2, we consider the realization of the Chrestenson ($\mathbf{C_4}$) gate. The $\mathbf{C_4}$ gate is the 4-dimensional analog of the Hadamard gate, a beam splitter for two-dimensional qubits. A unitary transfer matrix for the $\mathbf{C_4}$ gate is:

$$\mathbf{C}_4 = \frac{1}{\sqrt{4}} \begin{bmatrix} 1 & 1 & 1 & 1 \\ 1 & i & -1 & -i \\ 1 & -1 & 1 & -1 \\ 1 & -i & -1 & i \end{bmatrix} \tag{1}$$

Functionally, each basis state component incident to the $\mathbf{C}_4$ gate is mixed to contribute equally to each output basis component in terms of their probability amplitudes. The induced phase shifts of this mixing ensure that the transfer matrix properly realizes the $\mathbf{C}_4$ operator as unitary so that energy is conserved. Because $\mathbf{C}_4$ is a normalized four-dimensional discrete Fourier transform (DFT) matrix, it can be easily expanded into a higher D-dimensional form, $\mathbf{C}_D$, through use of the well-known DFT matrix properties as shown in Eqs. 2 and 3.

$$w_m^k = e^{i\frac{2\pi km}{D}} \tag{2}$$

$$\mathbf{C}_D = \frac{1}{\sqrt{D}} \begin{bmatrix} w_0^0 & w_1^0 & \cdots & w_{D-1}^0 \\ w_0^1 & w_1^1 & \cdots & w_{D-1}^1 \\ \vdots & \vdots & \ddots & \vdots \\ w_0^{D-1} & w_1^{D-1} & \cdots & w_{D-1}^{D-1} \end{bmatrix} \tag{3}$$

For the case of path-encoded qudits, a LTI 4-port coupler can be used to implement the $\mathbf{C}_4$ operator [16][17][18]. However, the basis state components for a multicolor photon's quantum state are the colors, or energies/frequencies, of the photon. Hence, mixing is achieved by driving the MZMs with the appropriate electrical RF waveforms. In this example, we drive each branch modulator within the MZM with an RF signal that is conveniently represented as a three-term Fourier series,

$$m(t) = a_1\cos(\omega_{\mathrm{m1}}t+\phi_1)+a_2\cos(\omega_{\mathrm{m2}}t+\phi_2)+a_3\cos(\omega_{\mathrm{m3}}t+\phi_3), \tag{4}$$

that causes the MZM to spread each basis state amplitude component from one color to the others. In this work, we define our modulation signals as $\omega_{\mathrm{m1}} = \delta$, $\omega_{\mathrm{m2}} = 2\delta$, and $\omega_{\mathrm{m3}} = 3\delta$, where δ is the RF frequency of the Free Spectral Range (FSR) defining the pure state structure of the frequency-encoded qudit of interest. An electro-optical phase modulator (EOM) is typically used in multicolor photon quantum processing [10, 12, 13]. When a three-tone modulation signal, $m(t)$, of the form of Eq. (4) is applied to the EOM, an optical input denoted as $E(t)$ produces a Bessel series output $E_{out}(t)$ of the form,

$$\begin{aligned} E_{out}(t) = \sum_{n=-\infty}^{\infty}\sum_{m=-\infty}^{\infty}\sum_{k=-\infty}^{\infty} & J_n(\beta_1)J_m(\beta_2)J_k(\beta_3) \\ & \times\cos(\omega_c t + n\omega_{\mathrm{m1}}t + m\omega_{\mathrm{m2}}t + k\omega_{\mathrm{m3}}t \\ & + n\phi_1 + m\phi_2 + k\phi_3) \end{aligned} \tag{5}$$

A Mach Zhender Modulator (MZM) comprises two such phase modulators, one in an upper arm and the other in a lower arm. The use of an MZM over a single arm phase modulator provides more degrees of freedom that can be used to enhance the performance of the gate. If one desires more such control, then additional MZM arms may be deployed. The nested MZM consists of two MZIs arranged inside a larger one, and allows for more precise control of phase shifts and interference patterns, enabling enhanced modulation and filtering capabilities. For example, the nested MZM structure is widely used in modern coherent photonic communication systems; a nested MZM can form any desired Quadrature Amplitude Modulated (QAM) state [19]. .

IV. Numerical Optimization

A. Particle Swarm Optimization

Particle Swarm Optimization (PSO) is a commonly used statistical optimization technique designed to minimize a cost function by mimicking the behavior of flocking birds, whose flight patterns are influenced by both the individual bird's

location and information shared throughout the flock. In systems, the "birds" are implemented as "particles" which travel through an n-dimensional space and velocities calculated based on each particle's inertia and position, as well as the position of the most optimized particle in the system, as introduced in [24]

The cost function contains two terms that simultaneously focus on the desirable in-band spectral lines and the undesirable out-of-band spectral lines or "leakage." For the in-band components, we employ Eq. (5) to calculate the output of the nested MZM and use a PSO to minimize the Frobenius norm among the ideal $\mathbf{C}_4$ transfer matrix and that obtained from the circuit. This portion of the cost function, c_{in}, is applied to the in-band spectral components and is shown in Eq. 6.

$$c_{in} = |\mathbf{C}_4 - \mathbf{T}_{circ}|^2 \tag{6}$$

The out-of-band cost, c_{out}, is also minimized simultaneously with the overall PSO cost function, $c_{pso} = cin + c_{out}$ being minimized. The leakage is computed as the energy or squared amplitude for the out-of-band spectral lines and the out-of-band cost, c_{out}, is just the sum of all the leakages. We set a PSO with a self-inertia of 0.5 and a swarm-inertia of 1.5 for 2,080 particles across 10,400 iterations to obtain the parameter values that produce results closest to the desired amplitude and phase of the in-band frequency sidebands, while minimizing probability amplitudes in the other sidebands due to the c_{out} term in the cost function. These 26 parameters consist of 12 modulation strengths, 12 modulation phases, and 2 bias phases for the MZMs. As an example of the structure of the PSO parameter search process, consider the first column vector in $\mathbf{C}_4$, which is $(\frac{1}{\sqrt{4}})[1\ 1\ 1\ 1\ ]^{\mathrm{T}}$. This portion of the $\mathbf{C}_4$ matrix is responsible for generating the ideal response for the $|0\rangle$ component of the output photon's quantum state. This column vector indicates that the amplitude of the output spectral lines for $[\omega_0\ \omega_1\ \omega_2\ \omega_3]^{\mathrm{T}}$, which correspond to the $|0\rangle$ component of the ideal circuit response state $|\Psi_{out}\rangle$, should all be of equal amplitude and with no induced phase shift since these particular $\mathbf{C}_4$ matrix components are all real and of the same amplitude for this column vector. Every column vector of $\mathbf{C}_4$ is non-zero and has an equal amplitude of $\frac{1}{\sqrt{4}}$, thus the ideal output response for every component of $\mathbf{C}_4$ should equally spread the amplitude of the incident photons $|i\rangle$ basis component for all $\{i|i = 0, 1, 2, 3\}$. Induced phase shifts are either $\{0, \frac{\pi}{2}, \pi, \frac{3\pi}{2}\}$ corresponding to the normalized $\mathbf{C}_4$ matrix components $\{1, i, -1, -i\}$ respectively. Using the PSO methods in MATLAB's PSO toolbox [21], we obtain optimized values for the 26 variables arising from the nested MZM structures that comprise the parallel branches of the QQFP shown in Figure 1 resulting in the targeted frequency sidebands and desired amplitude and phase values shown in Figure 2. For the second parallel nested MZM branch from the top in Figure 1, that corresponds to the second column vector of the $\mathbf{C}_4$ in the QQFP gate, the order of the targeted frequency sidebands is mapped to the frequency spectrum components at indices $[-1, 0, 1, 2]$ in Figure 3. All of these spectral lines should have equal amplitude in the ideal case and their phases should shift by $\left[0, \frac{\pi}{2}, \pi, \frac{3\pi}{2}\right]$ respectively that corresponds to the normalized second column vector of $\mathbf{C}_4$ which is $[1\ i\ -1\ -i]^{\mathrm{T}}$. The resulting amplitude and phase of the targeted frequency bins obtained through PSO optimization are shown in Figure 3. Similarly, for the third parallel nested MZM branch from the top in Figure 1, that corresponds to the third column vector of the $\mathbf{C}_4$ in the QQFP gate, the order of the targeted frequency sidebands is mapped to the frequency spectrum components at indices $[-2, -1, 0, 1]$ in Figure 4. All of these spectral lines should have equal amplitude in the ideal case and their phases should shift by $[0, \pi, 0, \pi]$ respectively that corresponds to the third normalized column vector of $\mathbf{C}_4$ which is $[1\ -1\ 1\ -1]^{\mathrm{T}}$. The resulting amplitude and phase of the targeted frequency bins obtained through PSO optimization are shown in Figure 4. And finally, for the fourth parallel nested MZM branch from the top in Figure 1, that corresponds to the fourth column vector of the $\mathbf{C}_4$ in the QQFP gate, the order of the targeted frequency sidebands is mapped to the frequency spectrum components at indices $[-3, -2, -1, 0]$ in Figure 5. All of these spectral lines should have equal amplitude in the ideal case and their phases should shift by $\left[0, \frac{3\pi}{2}, \pi, \frac{\pi}{2}\right]$ respectively that corresponds to the fourth normalized column vector of $\mathbf{C}_4$ which is $[1\ -i\ -1\ i]^{\mathrm{T}}$. The resulting amplitude and phase of the targeted frequency bins obtained through PSO optimization are shown in Figure 5. For the implementation of PSO, we use a high performance computing system to optimize the cost function across 104 dimensions corresponding to the four sets of 26 parameters for each MZM. These results produce gate fidelities in excess of 0.995, with gate fidelity defined as Eq. 7 where $\boldsymbol{\rho}$ and $\boldsymbol{\sigma}$ are the density matrices of the ideal and QQFP gate respectively [25].

$$F(\boldsymbol{\rho}, \boldsymbol{\sigma}) = \left(\mathrm{Tr}\sqrt{\sqrt{\boldsymbol{\rho}}\boldsymbol{\sigma}\sqrt{\boldsymbol{\rho}}}\right)^2 \tag{7}$$

Running PSO for a set of 104 parameters with a large number of particles over many iterations is computationally intensive and warranted the use of high performance computing. However, similar results can be obtained with significantly less processing power by solving for each MZM's 26 parameters individually and utilizing the linearity of the columns in the QQFP gate to find a column-wise fidelity. These column fidelities can then be averaged to find the overall gate fidelity as defined in Eq. 8.

$$F(\boldsymbol{\rho}, \boldsymbol{\sigma}) = \frac{1}{d}\sum_{i=1}^{d} |\langle\psi_{i\boldsymbol{\rho}}|\psi_{i\boldsymbol{\sigma}}\rangle|^2 \tag{8}$$

where d is the dimension of the qudit and ψ_i is the i^{th} column vector of the density matrices. Working with column-wise optimization also requires a modification of the cost function to prevent distinct and differing global phase factors from being applied to each column's result as a side-effect of the cost minimization, an effect that was irrelevant to gate-wise optimization. A cost penalty of the form $\frac{1}{2}(1 - cos(\theta))$ can be

added to the cost function while optimizing and should be removed before the final fidelity calculation, which successfully prevents undesirable column phase shifts without degrading the final fidelity results. Optimizing the gate's fidelity using the column-wise implementation only affected the third significant digit of the best fidelity results and used significantly less computing power and runtime.

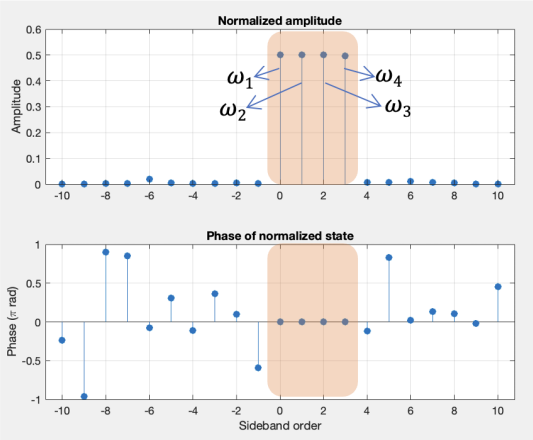

Fig. 2: Generated sidebands of the first mixer corresponding to the first column of the $\mathbf{C}_4$ gate, showing their targeted amplitudes and phases. The 26 mixer parameters are obtained using PSO.

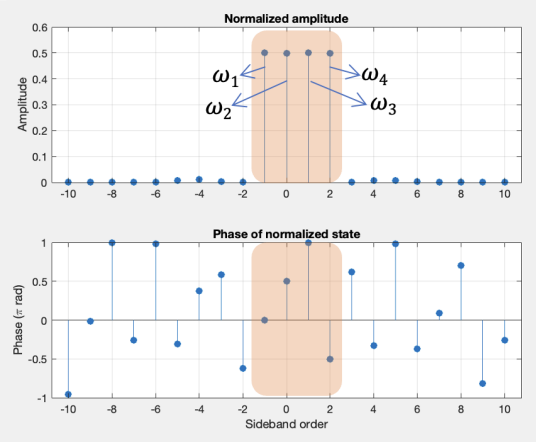

Fig. 3: Generated sidebands of the second mixer corresponding to the second column of the $\mathbf{C}_4$ gate, showing their targeted amplitudes and phases. The 26 mixer parameters are obtained using PSO.

V. Sensitivity Analysis

In practical quantum photonic integrated circuits, fabrication tolerances, environmental fluctuations, and control inaccuracies can introduce variations in device parameters, potentially degrading gate performance. To assess the robustness of our parallel nested MZM architecture, we perform a sensitivity analysis using Monte Carlo simulations that allow for all parameters to simultaneously vary. This evaluates how parameter perturbations affect the gate fidelity, providing insights into the

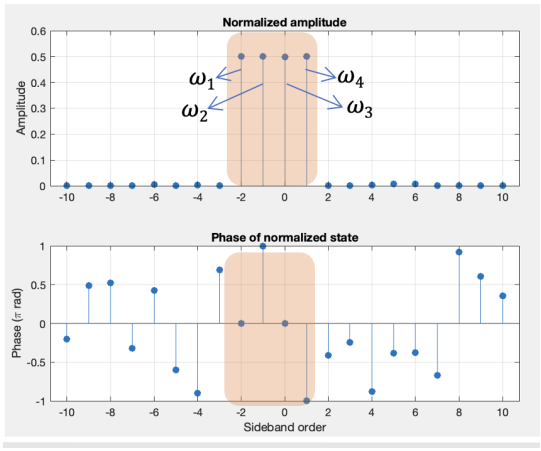

Fig. 4: Generated sidebands of the third mixer corresponding to the third column of the $\mathbf{C}_4$ gate, showing their targeted amplitudes and phases. The 26 mixer parameters are obtained using PSO.

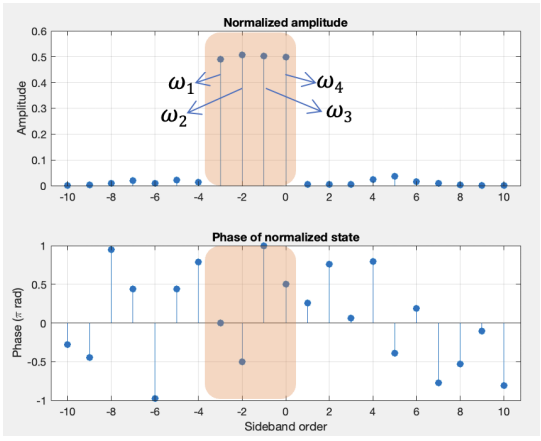

Fig. 5: Generated sidebands of the fourth mixer corresponding to the fourth column of the $\mathbf{C}_4$ gate, showing their targeted amplitudes and phases. The 26 mixer parameters are obtained using PSO.

design's tolerance to real-world imperfections. The analysis focuses on a four-dimensional gate, comprising four nested MZMs (one per dimension or "column"), each defined by 26 parameters: 12 modulation depths β (three per arm across four arms), 12 drive phases ϕ (matching the β structure), and two bias phases ($\phi_{\text{bias,I}}$ and $\phi_{\text{bias,Q}}$). Thus, the full gate uses 104 parameters. We use optimized parameter sets obtained via numerical minimization of a cost function based on the overlap fidelity between target and actual frequency comb states. For the Monte Carlo simulation, each parameter is independently perturbed with additive Gaussian noise. For non-zero nominal values, the noise has zero mean and standard deviation equal to 2% of the nominal value; for zero-valued parameters, the deviation is an absolute 0.02 (scaled equivalently). We conduct 100,000 trials, computing the fidelity for each column in every trial using the squared modulus of the inner product between normalized target and actual state vectors, as defined

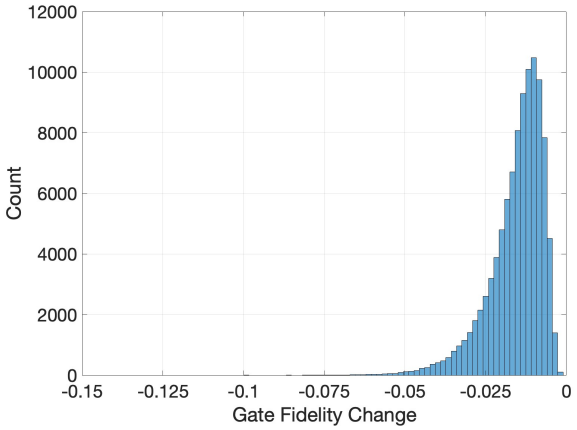

Fig. 6: Histogram of gate fidelity changes over 100,000 trials when **only phase** parameters (a subset of 48 parameters) are perturbed via Gaussian noise with standard deviation set to 2% of the nominal value.

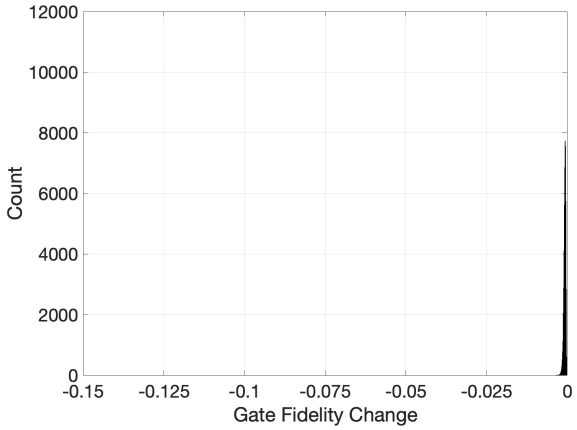

Fig. 7: Histogram of gate fidelity changes over 100,000 trials when **only modulation strength** parameters (a subset of 48 parameters) are perturbed via Gaussian noise with standard deviation set to 2% of the nominal value.

in the cost function. The gate fidelity is the average of the four column fidelities as previously described. This approach reveals the distribution of fidelity changes, highlighting the architecture's resilience. For instance, with all parameters varied, the mean fidelity change is typically small, indicating graceful degradation under moderate perturbations. Results are visualized through histograms of gate and per-column fidelity variations, aiding in identifying sensitive parameters for targeted improvements in future designs.

In Figure 6, we present the results of the gate-level sensitivity analysis for a $\mathbf{C}_4$ gate with Gaussian perturbation of only the modulation strength parameters, holding all other parameters constant at their optimized values. We report a mean fidelity change of -0.015534, standard deviation of 0.008545, and a minimum fidelity of 0.898959.

In Figure 7, we present the results of the gate-level sensitivity analysis for a $\mathbf{C}_4$ gate with Gaussian perturbation of only the modulation strength parameters, holding all other parameters constant at their optimized values. We report a mean fidelity change of -0.000796, standard deviation of 0.000326, and a minimum fidelity of 0.995013.

Taken together, the results of Figures 6 and 7 show that phase errors in the RF drive signals are far more important to control than amplitudes.

VI. Conclusions

Multicolor photons are an attractive proposition because of their potential to support high-dimensional states, and thus multivalued quantum logic. The parallel design facilitates scalability to similarly higher dimensions, as additional mixers can be incorporated without fundamental redesign, enabling processing of qudits with arbitrary dimensionality limited only by practical integration constraints. The scaling of a Hadamard (beamsplitter) for two-dimensional qubits to a Chrestenson ($\mathbf{C_4}$) gate serves as an illustration of this progression to higher dimension. More modulators in parallel may be added as the qudit dimension increases.

We have introduced a new arrangement of mixers and filters to process multicolor quantum states in this paper. If previous quantum processors are viewed as a serial cascade of mixers and filters [5, 8–15], the arrangement here may be considered to be parallel. In previous realizations, the modulator and filtering is separated into distinct stages. Here, these two stages are combined. The mixers here are conceptually placed between the demux/mux gratings of the programmable filters in references [5, 10–15]. Moreover, in this work, the single arm phase modulators are replaced with MZMs. Again, filtering is combined with mixing, and additional degrees of freedom are included in the processor. The parallel configuration offers an advantage with respect to parasitic (coupling) losses. In a serial architecture, parasitic losses cascade multiplicatively. A parallel arrangement, however, distributes one parasitic loss across each component so that, after the mux, only a single parasitic loss term is present. The architecture introduced here lends itself as well to photonic integration. Sources, demultiplexers, modulators and multiplexers may be realized in a thin-film lithium-niobate (TFLN) material system. This architecture extends naturally to other gates beyond the $\mathbf{C_4}$, such as $\mathbf{S}$, $\mathbf{X}$, $\mathbf{Z}$, and $\mathbf{T}$ gates, or any arbitrary unitary operation by adjusting the RF modulation parameters and mixer configurations. Using the same generic cell in an integrated fabric suggests a quantum field programmable photonic gate array (q-FPPGA) that operates on MVL. In summary of results, this paper has introduced a novel parallel architecture for realizing quantum gates in frequency-comb qudit systems, demonstrated through the implementation of the Chrestenson ($\mathbf{C_4}$) gate using both numerical optimization via particle swarms and an analytic approximation based on three-term truncated Fourier series. The approach leverages nested Mach-Zehnder modulators to achieve the required mixing of frequency components, with

sensitivity analysis highlighting robust operational regimes against parameter variations.

REFERENCES

[1] L. Olislager, "Frequency-bin entangled photons," Phys. Rev. A, vol. 82, no. 1, Jul. 2010.

[2] M. Chen, N. C. Menicucci, and O. Pfister, "Experimental realization of multipartite entanglement of 60 modes of a quantum optical frequency comb," Phys. Rev. Lett., vol. 112, no. 12, Mar. 2014.

[3] Roslund, J., de Araújo, R., Jiang, S. et al. Wavelength-multiplexed quantum networks with ultrafast frequency combs. Nature Photon 8, 109–112 (2014). https://doi.org/10.1038/nphoton.2013.340

[4] Kobayashi, T., Ikuta, R., Yasui, S. et al. Frequency-domain Hong–Ou–Mandel interference. Nature Photon 10, 441–444 (2016). https://doi.org/10.1038/nphoton.2016.74

[5] Kues, M., Reimer, C., Roztocki, P. et al. On-chip generation of high-dimensional entangled quantum states and their coherent control. Nature 546, 622–626 (2017). https://doi.org/10.1038/nature22986

[6] Mahmudlu, H., Johanning, R., van Rees, A. et al. Fully on-chip photonic turnkey quantum source for entangled qubit/qudit state generation. Nat. Photon. 17, 518–524 (2023). https://doi.org/10.1038/s41566-023-01193-1

[7] Clementi, M., Sabattoli, F.A., Borghi, M. et al. Programmable frequency-bin quantum states in a nano-engineered silicon device. Nat Commun 14, 176 (2023). https://doi.org/10.1038/s41467-022-35773-6

[8] S. E. Harris, "Nonlocal modulation of entangled photons," Phys. Rev. A, vol. 78, no. 2, Aug. 2008.

[9] S. Sensarn, G. Y. Yin, and S. Harris, "Observation of nonlocal modulation with entangled photons," Phys. Rev. Lett., vol. 103, no. 16, Oct. 2009.

[10] J. Lukens and P. Lougovski, "Frequency-encoded photonic qubits for scalable quantum information processing," Optica 4, 8-16 (2017).

[11] Poolad Imany, Jose A. Jaramillo-Villegas, Ogaga D. Odele, Kyunghun Han, Daniel E. Leaird, Joseph M. Lukens, Pavel Lougovski, Minghao Qi, and Andrew M. Weiner, "50-GHz-spaced comb of high-dimensional frequency-bin entangled photons from an on-chip silicon nitride microresonator," Opt. Express 26, 1825-1840 (2018)

[12] H.-H. Lu, "Electro-optic frequency beam splitters and tritters for high-fidelity photonic quantum information processing," Phys. Rev. Lett., vol. 120, no. 3, Jan. 2018

[13] Kues, M., Reimer, C., Lukens, J.M. et al. Quantum optical microcombs. Nature Photon 13, 170–179 (2019). https://doi.org/10.1038/s41566-019-0363-0

[14] Lu, HH., Lukens, J.M., Williams, B.P. et al. A controlled-NOT gate for frequency-bin qubits. npj Quantum Inf 5, 24 (2019). https://doi.org/10.1038/s41534-019-0137-z.

[15] Hsuan-Hao Lu, Marco Liscidini, Alexander L Gaeta, Andrew M Weiner, Joseph M Lukens, Frequency-bin photonic quantum information, Optica 2023

[16] MacFarlane, D. L., J. Tong, C. Fadadia, V. Govindan, L. R. Hunt and I. Panahi, "Extended lattice filters enabled by four-directional couplers," Appl. Opt., Vol. 43, No. 33, 6124-6133, 2004. Accessed on: May 27, 2025, doi: https://doi.org/10.1364/AO.43.006124, [Online].

[17] Duncan L MacFarlane, Marc P Christensen, Ke Liu, Tim P LaFave, Gary A Evans, Nahid Sultana, TW Kim, Jiyoung Kim, Jay B Kirk, Nathan Huntoon, Andrew J Stark, Mieczyslaw Dabkowski, Louis R Hunt, Viswanath Ramakrishna, "Four-port nanophotonic frustrated total internal reflection coupler," IEEE Photonics Technology Letters 21, 58-60 (2011).

[18] Kaitlin N Smith, Tim P LaFave, Duncan L MacFarlane, Mitchell A Thornton, "A radix-4 Chrestenson gate for optical quantum computation," 2018 IEEE 48th International Symposium on Multiple-Valued Logic (ISMVL) pp260-265 (2018).

[19] P. J. Winzer and R. . -J. Essiambre, "Advanced Optical Modulation Formats," in Proceedings of the IEEE, vol. 94, no. 5, pp. 952-985, May 2006, doi: 10.1109/JPROC.2006.873438. keywords: Optical modulation;Optical fiber networks;Optical crosstalk;Optical filters;Optical noise;Stimulated emission;Optical fiber polarization;Wavelength division multiplexing;Optical fiber communication;Web and internet services;Differential phase modulation;digital modulation;intensity modulation;optical communication;optical networks;wavelength division multiplexing (WDM),

[20] J.H. Holand, "Adaptation in Natural and Artificial Systems," MIT Press, 1992, ISBN 978-0262275552.

[21] MathWorks, "Particle Swarm Optimization User's Guide," The MathWorks, Inc., 2024. [Online]. Available: https://www.mathworks.com/help/gads/particle-swarm.html. [Accessed: Sep. 22, 2025].

[22] J. Ange, M. Tuller, J. M. Henderson, E. R. Henderson, B. A. Moores, D. L. MacFarlane, and M. A. Thornton, "Modeling and Simulation of Multiple-Valued and Nonlinear Quantum Photonic Components," in *2025 IEEE 55th International Symposium on Multiple-Valued Logic (ISMVL)*, 2025, pp. 123–128, doi: 10.1109/ISMVL64713.2025.00032.

[23] A. Muthukrishnan and C. R. Stroud, "Multivalued logic gates for quantum computation," *Phys. Rev. A*, vol. 62, no. 5, p. 052309, Oct. 2000, doi: 10.1103/PhysRevA.62.052309.

[24] James Kennedy and Russell C. Eberhart, "Particle Swarm Optimization," in *Proceedings of the IEEE International Conference on Neural Networks (ICNN)*, vol. 4, pp. 1942–1948, Perth, Australia, 1995.

[25] Jozsa, R. (1994). "Fidelity for Mixed Quantum States." Journal of Modern Optics, 41(12), 2315–2323. https://doi.org/10.1080/09500349414552171 (1994)